JPhys Materials

PAPER • OPEN ACCESS

Ultrafast photo-induced phonon hardening due to Pauli blocking in $MAPbI_3$ single-crystal and polycrystalline perovskites

To cite this article: Chelsea Q Xia *et al* 2021 *J. Phys. Mater.* **4** 044017

View the article online for updates and enhancements.

This content was downloaded from IP address 128.178.106.62 on 24/09/2021 at 13:09

IOP Publishing J. Phys. Mater. 4 (2021) 044017 https://doi.org/10.1088/2515-7639/ac22b9

Journal of Physics: Materials

OPEN ACCESS

RECEIVED
12 May 2021

REVISED
23 July 2021

ACCEPTED FOR PUBLICATION
1 September 2021

PUBLISHED
22 September 2021

Original Content from this work may be used under the terms of the Creative Commons Attribution 4.0 licence.

Any further distribution of this work must maintain attribution to the author(s) and the title of the work, journal citation and DOI.

PAPER

Ultrafast photo-induced phonon hardening due to Pauli blocking in $MAPbI_3$ single-crystal and polycrystalline perovskites

Chelsea Q Xia[1], Samuel Poncé[2,3], Jiali Peng[4], Aleksander M Ulatowski[1], Jay B Patel[1], Adam D Wright[1], Rebecca L Milot[5], Hans Kraus[6], Qianqian Lin[4], Laura M Herz[1,7], Feliciano Giustino[2,8,9] and Michael B Johnston[1,*]

[1] Department of Physics, University of Oxford, Clarendon Laboratory, Parks Road, Oxford OX1 3PU, United Kingdom
[2] Department of Materials, University of Oxford, Parks Road, Oxford OX1 3PH, United Kingdom
[3] Theory and Simulation of Materials (THEOS), École Polytechnique Fédérale de Lausanne, CH-1015 Lausanne, Switzerland
[4] Key Lab of Artificial Micro- and Nano-Structures of Ministry of Education of China, School of Physics and Technology, Wuhan University, Wuhan 430072, People's Republic of China
[5] Department of Physics, University of Warwick, Gibbet Hill Road, Coventry CV4 7AL, United Kingdom
[6] Department of Physics, University of Oxford, Denys Wilkinson Building, Keble Road, Oxford OX1 3RH, United Kingdom
[7] TUM Institute for Advanced Study , 85748 Garching bei München, Germany
[8] Oden Institute for Computational Engineering and Sciences, The University of Texas at Austin, Austin TX 78712, United States of America
[9] Department of Physics, The University of Texas at Austin, Austin, TX 78712, United States of America
[*] Author to whom any correspondence should be addressed.

E-mail: michael.johnston@physics.ox.ac.uk

Keywords: terahertz, phonon, lead halide perovskite, photovoltaics

Supplementary material for this article is available online

Abstract

Metal-halide perovskite semiconductors have attracted intense interest over the past decade, particularly for applications in photovoltaics. Low-energy optical phonons combined with significant crystal anharmonicity play an important role in charge-carrier cooling and scattering in these materials, strongly affecting their optoelectronic properties. We have observed optical phonons associated with Pb–I stretching in both $MAPbI_3$ single crystals and polycrystalline thin films as a function of temperature by measuring their terahertz conductivity spectra with and without photoexcitation. An anomalous bond hardening was observed under above-bandgap illumination for both single-crystal and polycrystalline $MAPbI_3$. First-principles calculations reproduced this photo-induced bond hardening and identified a related lattice contraction (photostriction), with the mechanism revealed as Pauli blocking. For single-crystal $MAPbI_3$, phonon lifetimes were significantly longer and phonon frequencies shifted less with temperature, compared with polycrystalline $MAPbI_3$. We attribute these differences to increased crystalline disorder, associated with grain boundaries and strain in the polycrystalline $MAPbI_3$. Thus we provide fundamental insight into the photoexcitation and electron–phonon coupling in $MAPbI_3$.

1. Introduction

Metal-halide perovskite (MHP) semiconductors have emerged as promising materials for future photovoltaic applications [1, 2] owing to their outstanding optoelectronic properties including high charge-carrier mobilities and long diffusion lengths [3–7]. There is currently debate on the importance of crystal anharmonicity and electron–phonon interactions in determining the electronic and other physical properties of MHPs [8, 9]. A harmonic crystal has a potential energy which is quadratic as a function of nuclear coordinates, which in any real crystal is only a good approximation for small nuclear displacements. Thus all crystals are anharmonic to some extent, but the degree of anharmonicity varies with the material. Given that thermal expansion is directly related to anharmonicity, the large linear thermal expansion coefficient of the prototypical MHP, $CH_3NH_3PbI_3$ ($MAPbI_3$), [10] suggests that anharmonicity is particularly large and thus plays a significant role in the electronic properties of this material.

© 2021 The Author(s). Published by IOP Publishing Ltd

An understanding of the phonon dispersion relation and electron–phonon coupling [11] in $MAPbI_3$ is therefore key to gaining a full understanding of its technologically significant physical properties, such as its charge-carrier mobility [6, 12]. Previously Raman and infrared (IR) spectroscopy studies have been performed on $MAPbI_3$ covering the spectral range 30–3700 cm^{-1}, from which the phonon absorption peaks were assigned to the internal vibrations of the MA^+ cations, the cation librations or the internal vibrations of the PbI_3 framework [13–17]. Meanwhile, computational studies based on first-principles calculations have been conducted on $MAPbI_3$ in the low-temperature regime (orthorhombic phase), allowing their theoretical phonon dispersion relations to be revealed [18, 19]. Thus, phonons in $MAPbI_3$ have already been extensively studied both experimentally and theoretically, allowing a comprehensive assignment of nuclear motion to observed modes. However, there are no substantial studies investigating how phonon modes are affected by photoexcitation or studies comprehensively comparing the phonon spectra of $MAPbI_3$ single crystals with those of polycrystalline thin films.

In this work, we first performed terahertz (THz) spectroscopy on $MAPbI_3$ thin films and single crystals to measure AC conductivity spectra and thus study phonon modes associated with Pb–I stretching. Phonon spectra were recorded at temperatures ranging from 5 to 300 K covering the orthorhombic and tetragonal phases of $MAPbI_3$. By photoexciting the $MAPbI_3$ single crystal and thin film using an ultrafast laser pulse at photon energy 3.1 eV, a phonon blue-shift effect was observed. This contrasts with the red-shift of phonon modes observed when most conventional semiconductors such as bismuth, silicon and germanium are photoexcited, owing to the anharmonicity of their lattice potential [20–22]. Since the blue-shift observed in our experiment happens on an ultrafast timescale (within 5 ps of pulsed photoexcitation), its origin is likely to be an electronic process. Using *ab initio* bandstructure calculations we show it to be the result of Pauli blocking, rather than a much slower photostriction process associated with the orientation of the organic cations [23, 24]. A direct comparison of the optical phonon spectra of single-crystal and polycrystalline $MAPbI_3$ revealed a much narrower linewidth and longer phonon lifetime for single crystal samples. The phonon lifetimes in single crystal $MAPbI_3$ were attributed to anharmonicity and optical phonon–electron (i.e. Fröhlich) interactions. While these mechanisms are also important in polycrystalline $MAPbI_3$ we attribute the observed additional line broadening and shorter phonon lifetimes to increased crystalline disorder, associated with grain boundaries and strain.

2. Results and discussion

To gain better insight into the importance of phonon modes and anharmonicity in $MAPbI_3$ we chose to compare high-quality single crystals with polycrystalline thin films used in high-efficiency photovoltaic devices. Free-standing single crystals of $MAPbI_3$ were grown by inverse temperature crystallization using a previously published method [25, 26]. The resulting crystals had large (10 mm $\times$ 10 mm) mirror-like facets which were ideal for precise THz spectroscopy. Optically smooth polycrystalline $MAPbI_3$ thin films were grown to a thickness of 600 nm on z-cut quartz substrates by vapor co-deposition [27, 28]. The growth parameters matched those used to produce solar cells with over 19% power conversion efficiency [29]. SEM images and XRD spectra taken on the single crystals and polycrystalline thin films were previously published in [7]. All samples were stored in a nitrogen glove box prior to measurements. Further details of the sample growth and preparation are provided in the section 4.

Optical phonon modes of $MAPbI_3$ associated with internal vibrations of the PbI_3 framework occur at THz frequencies, thus we studied their properties using a combination of THz time-domain spectroscopy (THz-TDS) and optical-pump–THz-probe spectroscopy (OPTPS). These measurements were performed in a vacuum chamber at a pressure of 10^{-6} mbar where the lattice temperature of the single crystals and thin films was controlled using a cold finger cryostat with a range 5–300 K. The ultra-low thermal conductivity of $MAPbI_3$ [30, 31] means in such a system extra care is required when determining sample temperature especially for free-standing single crystals under laser illumination. Therefore, the (100)-facet of the single crystal being studied was pressed onto a sapphire substrate that was in intimate contact with the cryostat cold finger. Even in this case, the lowest temperature attainable for the single crystal was 75 K for a cold-finger temperature of 5 K (the true temperature of the single crystal in the illuminated area was determined using a contact-free optical method, which is detailed in the section 4). In contrast, since the $MAPbI_3$ thin film was deposited directly on a quartz substrate, there was excellent thermal contact between the 600 nm film and the thermally conductive quartz, so the thin film could reach the minimum cold-finger temperature of 5 K.

To investigate the behavior of phonon modes of $MAPbI_3$ single crystals and thin films in different crystal phases, we measured their AC conductivity spectra as a function of lattice temperature in the absence of visible light with the cold-finger cryostat temperature increasing gradually from 5 to 300 K. In the case of the $MAPbI_3$ thin film, the 'dark' conductivity $\sigma_{\mathrm{dark}}(\omega)$ was calculated directly from the experimental THz transmission spectra according to [32, 33]

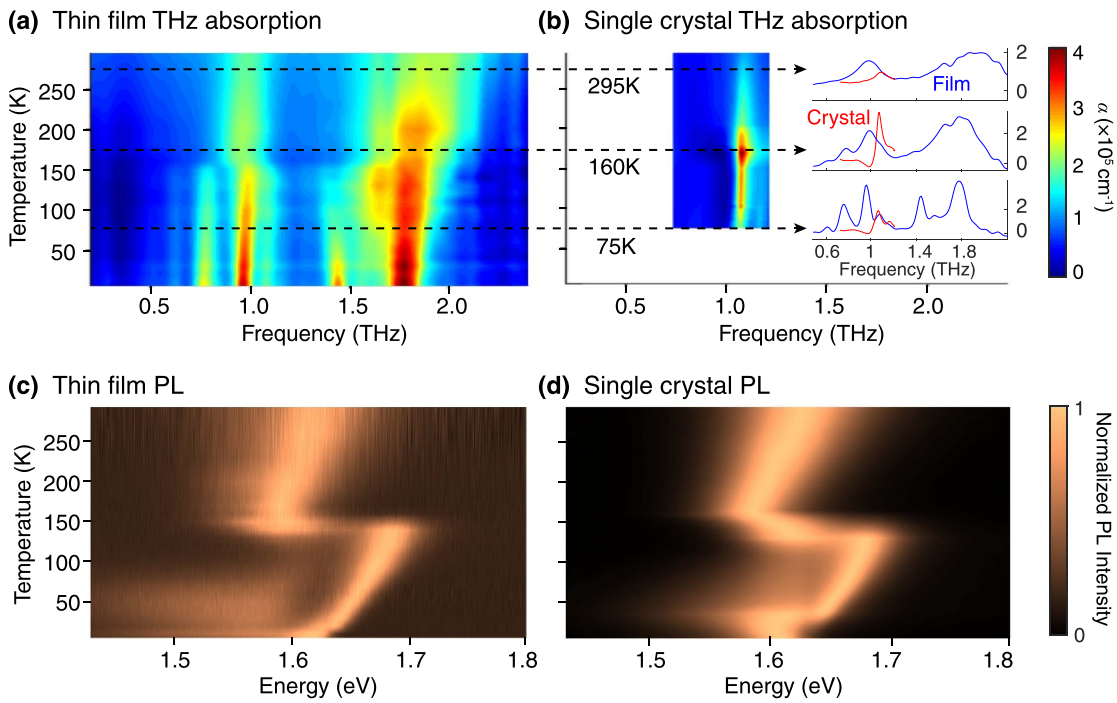

Figure 1. Temperature-dependent absorption spectra of $MAPbI_3$ (a) thin film and (b) single crystal measured in transmission and reflection modes respectively. The inset demonstrates a comparison in absorption between the thin film and single crystal at 75, 160 and 295 K. Temperature-dependent PL spectra of the (c) thin film (d) single crystal. All the THz-TDS measurements were performed using a cold-finger cryostat, with the true temperature of the single crystal determined using the PL-facilitated temperature correction technique (see section 4 for more details). The thin-film PL was also measured using a cold finger cryostat, but to gain an extended temperature range the PL from the single crystal was measured in a helium gas exchange cryostat.

$$\sigma_{\text{dark}}(\omega) = \frac{\varepsilon_0 c(1+\tilde{n}_s)}{d}\left(\frac{1}{\mathcal{T}(\omega)} - 1\right), \tag{1}$$

where ε_0 is the permittivity of free space, c is the speed of light, $\tilde{n}_s = 2.1$ is the refractive index of the quartz substrate at THz frequencies [34], and $d = 600$ nm is the thickness of the $MAPbI_3$ thin film. $\mathcal{T}(\omega) = T_{\text{sample}}(\omega)/T_{\text{reference}}(\omega)$ is the transmission function of THz electric field, where $T_{\text{sample}}(\omega)$ and $T_{\text{reference}}(\omega)$ are the THz electric field spectra of a THz pulse transmitted through a $MAPbI_3$ thin-film sample deposited on a quartz substrate and a bare quartz substrate respectively.

In the case of the single crystal, we performed THz-TDS in reflection rather than transmission geometry, owing to the limited transmission of THz pulses through a ~10 mm thick crystal. A schematic diagram of the THz-TDS system in transmission and reflection modes is provided in supplementary figure 1 (available online at stacks.iop.org/JPMATER/4/044017/mmedia). The THz reflectivity of the $MAPbI_3$ single crystal $r(\omega)$ was expressed in terms of its dielectric function $\varepsilon(\omega)$ as

$$r(\omega) = \tilde{r}_{\text{mirror}}(\omega)\left|\frac{R_{\text{crystal}}(\omega)}{R_{\text{mirror}}(\omega)}\right|^2 = \left|\frac{\sqrt{\varepsilon(\omega)}-1}{\sqrt{\varepsilon(\omega)}+1}\right|^2, \tag{2}$$

where $R_{\text{crystal}}(\omega)$ represents the reflected THz electric field measured from the crystal and $R_{\text{mirror}}(\omega)$ is the reflected THz field measured from a gold mirror which was used as a reference as gold has a reflectivity $\tilde{r}_{\text{mirror}}(\omega)$ very close to unity across the THz band [35]. The reflectivity spectrum was then fitted numerically using the method of variational dielectric functions (details given in the supplemental material), from which the THz absorption spectrum $\alpha(\omega)$ was extracted.

Figure 1 displays the THz absorption coefficient and photoluminescence (PL) spectra for both thin-film and single-crystal $MAPbI_3$ as a function of temperature. The THz absorption of thin-film $MAPbI_3$ displayed in figure 1(a) shows a series of absorption peaks associated with IR-active phonon modes. Four modes of large oscillator strength and three weaker modes are observed for temperatures below 75 K. With increasing temperature all modes gradually blueshift and become broader. Such a blue-shift is characteristic of anharmonicity while the phonon broadening has been attributed by Weller *et al* [36] to an enhanced positional disorder of the organic cation (MA^+) with increasing temperature. Furthermore, when the temperature reaches the orthorhombic-to-tetragonal phase transition temperature (~150 K), rotational

disorder of the MA^+ cation comes into play [37], which gives rise to an abrupt redshift of some phonon modes. The structural phase transition is also observed in temperature-dependent PL measurements shown in figure 1(c) where a well-known [11] sudden reduction of bandgap is seen at ∼150 K. The bandgap opens with increasing temperature below the phase transition at a rate of 0.46 meV K^{-1}, which drops to 0.33 meV K^{-1} above the phase transition (supplementary figure 4 shows the bandgap energy of $MAPbI_3$ thin film and single crystal as a function of temperature). Moreover, above the phase transition temperature, the phonon modes continue to broaden and eventually merge into two remaining phonon peaks at room temperature. The observations agree with previous THz-TDS studies on solution-processed $MAPbI_3$ [38] films, as well as $MAPbBr_3$ [39] films.

To date there have been few THz-TDS studies on the temperature dependence of phonon modes in single-crystal MHPs. Figure 1(b) shows the absorption coefficient of single-crystal $MAPbI_3$ as a function of frequency and temperature. Although the spectral range was limited by experimental constraints, one narrow phonon mode at ∼1.1 THz is observable, which is much narrower than any of the modes observed from the thin film. Significantly, for single crystal $MAPbI_3$, there is a strong enhancement of the oscillator strength of the ∼1.1 THz mode at the orthorhombic-tetragonal structural phase transition temperature (∼150 K) and a drop in oscillator strength at low temperatures (<100 K). Remarkably the frequency of this single-crystal phonon mode is temperature independent over the full temperature range, in stark contrast to the significant blue shifts seen in all the observed phonon modes of thin-film $MAPbI_3$ which have been associated with anharmonicity.

To compare the phonon modes between the single crystal and the thin film more quantitatively, we fitted the dark conductivity spectra with a sum of Lorentzian oscillators,

$$\sigma(\omega) = \varepsilon_0 \omega \sum_j^N \frac{f_j \omega_{\mathrm{TO},j}^2}{\mathrm{i}(\omega_{\mathrm{TO},j}^2 - \omega^2) + \gamma_{\mathrm{TO},j}\omega}, \tag{3}$$

where N is the number of phonon modes, $\omega_{\mathrm{TO},j}$ is the frequency of the jth transverse optical (TO) phonon mode with oscillator strength f_j and $\gamma_{\mathrm{TO},j}$ is the corresponding TO-phonon scattering rate (see the supplemental material for more details of the Lorentzian oscillator model). Figure 2 shows least-squares fits of equation (3) to the AC conductivity data obtained from THz-TDS at two temperatures. The model fits the THz-TDS transmission data particularly well at low temperature where the phonon modes are well separated, as can be seen in figure 2(a). A summary of the data extracted from the fit shown in figure 2 is provided in table 1.

According to the first-principles calculations performed by Pérez-Osorio *et al* [18] and by comparing the relative intensities between each phonon mode, the most prominent phonon peaks observed in the $MAPbI_3$ thin film with $\omega_{\mathrm{TO}} = 25.4$ and 31.7 cm^{-1} are assigned to the Pb–I stretching modes of B_u symmetry, whereas the phonon peaks with $\omega_{\mathrm{TO}} = 47.7$ and 58.0 cm^{-1} are assigned to libration/translation modes of the MA^+ cations (see figure 7(c) and table 6 in [18]).

Interestingly, it can be seen from the inset in figure 1(b) and table 1 that the phonon modes of single-crystal $MAPbI_3$ appear at slightly higher frequency than for the thin films, although it must be stressed that these differences are close to the spectral resolution of our experiment. This frequency shift might be related to differing levels of strain between the two morphologies [40, 41]. Nevertheless, by comparing the relative intensity between those phonon modes observed in the $MAPbI_3$ single crystal to that in the thin film within the frequency range of 0.5–1.4 THz, we conclude that the dominant phonon in the single crystal ($\omega_{\mathrm{TO}} = 35.3 cm^{-1}$) also comes from the Pb–I stretching mode.

We propose that the scattering rate of optical phonons (γ_{TO}) in pure single-crystal $MAPbI_3$ is primarily determined by a combination of scattering with electrons via the Frölich interaction and crystal anharmonicity [42]. Significantly, as can be seen in figure 1(b) we measured no significant shift of the ∼1.1 THz TO phonon frequency for single-crystal $MAPbI_3$ over a temperature range 75–295 K. Surprisingly, the only evidence of the orthorhombic-tetragonal structural phase transition (∼150 K) was an enhancement of the phonon mode oscillator strength, rather than the frequency shift seen for polycrystalline $MAPbI_3$ (in figure 1(a)). This contrast with the dramatic changes in the PL spectra (figures 1(c) and (d)) at the phase transition. Our observations are consistent with previous theoretical work which has shown low levels of anharmonicity in the (low temperature) orthorhombic phase of single-crystal $MAPbI_3$ [43]. Thus it is possible that Fröhlich scattering is the primary limit to phonon lifetime (γ_{TO}) in pure single-crystal $MAPbI_3$ and indicates that estimation of charge-carrier mobility from phonon spectra [38] may be reasonable in this case.

The much larger optical phonon linewidths and scattering rates (γ_{TO}) observed from polycrystalline $MAPbI_3$ can be attributed to the crystalline disorder in addition to the contributions also seen in single

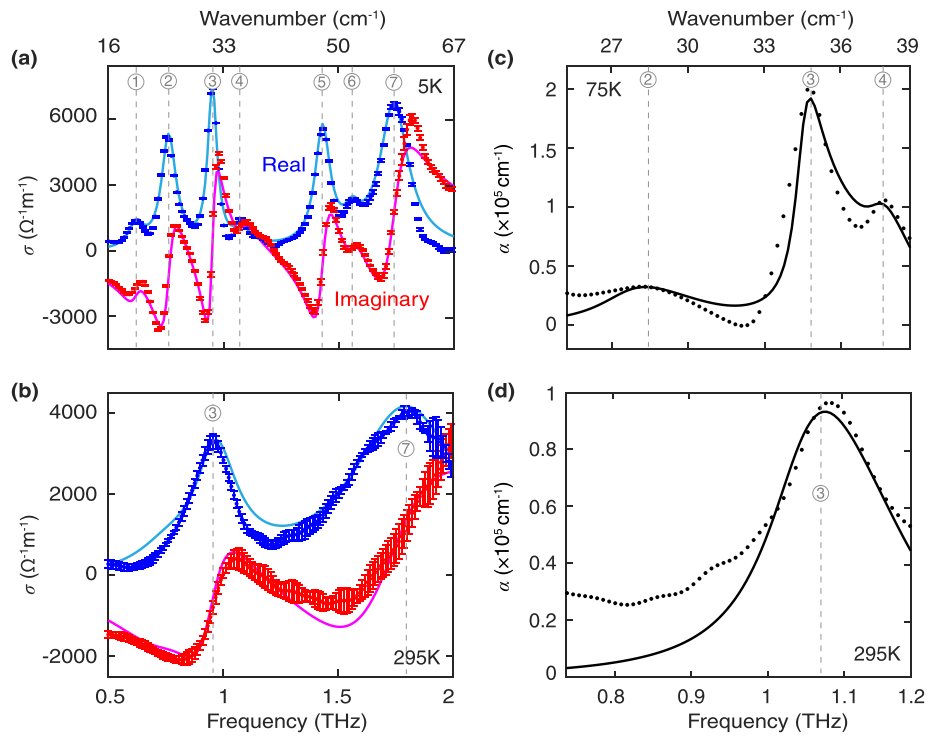

Figure 2. AC conductivity spectra of thin-film $MAPbI_3$ at (a) 5 K and (b) 295 K. The blue (red) points show the measured real (imaginary) conductivity, while the solid lines show fits to the data using a sum of Lorentzian oscillators according to equation (3). Error bars represent a single standard deviation random error determined from three repeat measurements. Absorption spectra of single crystal $MAPbI_3$ at (c) 75 K and (d) 295 K. The points represent the measured data and solid lines are fits to equation (2). The frequencies of the TO phonon modes listed in table 1 are indicated by the grey dashed lines and their mode assignments labeled by the circled grey numbers.

Table 1. Experimentally measured TO-phonon frequencies, ω_{TO}, and scattering rates, γ_{TO}, of thin-film and single-crystal $MAPbI_3$. The normalized oscillator strength is represented by $\tilde{f}_j = f_j/\sum_j f_j$ where j is the phonon mode index. †Rock, stretch, bend and libration refer to Pb–I–Pb rocking mode, Pb–I stretching mode, Pb–I–Pb bending mode and libration/translation modes of the MA^+ cations respectively. *Note that the true TO-phonon scattering rate of the single crystal measured at 75 K may be significantly smaller because the measurements were limited by the spectral resolution which was 0.3 cm^{-1}.

	Phonon mode index Mode assignment†		1 Rock	2 Stretch	3 Stretch	4 Bend	5 Libration	6 —	7 Libration
Thin film	ω_{TO} (cm^{-1})	5 K	20.7	25.4	31.7	36.0	47.7	52.0	58.0
	γ_{TO} (10^{12} s^{-1})	5 K	0.43	0.48	0.30	0.80	0.50	0.50	0.95
	$\tilde{f}_j$	5 K	0.08	0.30	0.23	0.60	0.15	0.04	0.14
	ω_{TO}	295 K	—	—	31.7	—	—	—	60.1
	γ_{TO}	295 K	—	—	1.30	—	—	—	3.50
	$\tilde{f}_j$	295 K	—	—	0.66	—	—	—	0.34
Single crystal	ω_{TO}	75 K	—	27.7	35.0	38.3	—	—	—
	γ_{TO}	75 K	—	0.40*	0.20*	0.30*	—	—	—
	$\tilde{f}_j$	75 K	—	0.30	0.55	0.15	—	—	—
	ω_{TO}	295 K	—	—	35.3	—	—	—	—
	γ_{TO}	295 K	—	—	0.70	—	—	—	—
	$\tilde{f}_j$	295 K	—	—	1	—	—	—	—

crystals from the Fröhlich interaction and crystal anharmonicity. Sources of structural disorder in polycrystalline MHPs are grain boundaries [7] and strain [44] as well as impurities and defects. While structural disorder will also affect charge transport, direct calculation of mobility from the phonon spectrum becomes challenging in this case.

In order to investigate the behavior of charge-carrier transport in $MAPbI_3$ single crystals and thin films and its relationship with phonon modes, we photoexcited them with 35 fs laser pulses of central wavelength 400 nm ($h\nu = 3.1$ eV) to generate charge carriers and measured the photoconductivity spectrum using OPTPS. The presence of free charge carriers leads to an increased conductivity of the semiconductor, which

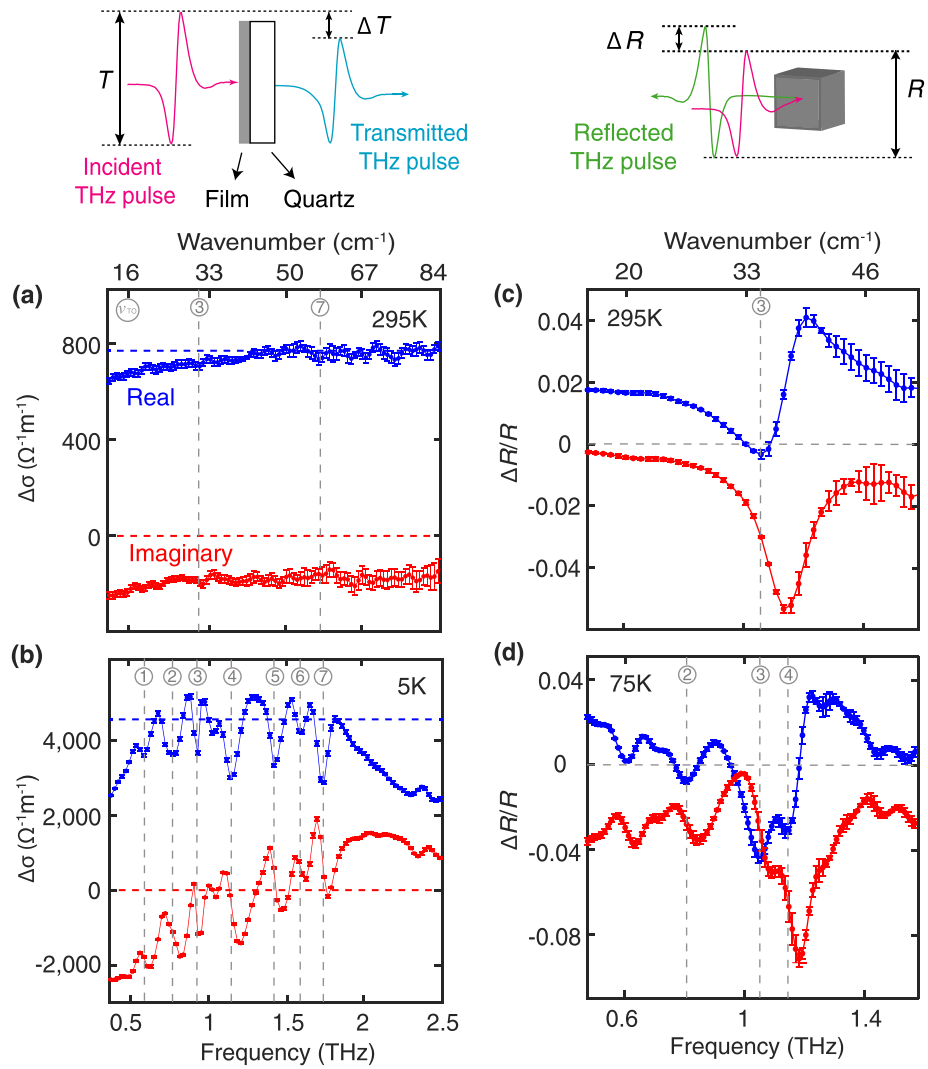

Figure 3. Photoconductivity spectra of $MAPbI_3$ thin film measured at 5 ps after photoexcitation at (a) 295 K and (b) 5 K in transmission. The blue and red dots represent experimental data of the real and imaginary parts of photoconductivity, whereas the blue and red dashed lines represent the Drude fit. Photoconductivity of $MAPbI_3$ single crystal measured at 5 ps after photoexcitation at (c) 295 K and (d) 75 K in reflection, expressed as ($\Delta R/R$). The frequencies of the TO phonon modes are listed in table 1, which were determined from the 'dark' photoconductivity measurements are indicated by the grey dashed lines and their mode assignments labeled by the circled grey numbers. The lines joining the data points are guides to the eye. The schematic diagrams at the top of the figure indicate the geometry of the OPTPS setup for the plots below them (i.e. transmission geometry for thin-film measurements and reflection geometry for single-crystal measurements). The photoconductivity spectra were taken at 5 ps after photoexcitation under fluence 48 μJ cm^{-2}.

causes a decrease (increase) of the transmission (reflection) of the THz conductivity probe pulse. Quantitatively, the THz photoconductivity measured in transmission may be expressed by [45, 46],

$$\Delta\sigma(\omega) = -\frac{\varepsilon_0 c(1+\tilde{n}_s)}{d}\left(\frac{\Delta T}{T_{\text{on}}}\right)\left(\frac{T_{\text{reference}}}{T_{\text{off}}}\right), \tag{4}$$

where $T_{\text{on (off)}}(\omega)$ is the THz electric field spectrum measured after transmission through the $MAPbI_3$ film on quartz with the laser on (off), and $\Delta T(\omega) = T_{\text{on}}(\omega) - T_{\text{off}}(\omega)$. As in equation (1), $T_{\text{reference}}(\omega)$ is the electric field spectrum measured after the THz has passed through the quartz substrate only.

The photoconductivity spectrum measured at 295 K and extracted via this expression is shown in figure 3(a). The flat non-zero real part of conductivity and near zero imaginary part are consistent with a free charge-carrier Drude response,

$$\Delta\sigma(\omega) = \sigma_{\text{Drude}} = \frac{ne\mu}{1 - \mathrm{i}\omega\tau}, \tag{5}$$

where n is the charge-carrier density determined by the photoexcitation fluence, e is the elementary charge, μ is the electrical mobility and τ is the charge-carrier momentum scattering time. The expected Drude

response for the measured initial mobility of charge carriers in the samples is shown by the blue and red dashed lines in figure 3(a), which shows reasonable agreement with the experimental data. The photoconductivity spectrum measured at 5 K (figure 3(b)), however, shows some phonon modulations on top of the Drude response, which is evidence for electron–phonon coupling in $MAPbI_3$.

In the case of $MAPbI_3$ single crystals, since the THz signal was measured in a reflection geometry, the photoconductivity is expressed in terms of $\Delta R/R$ as [47, 48],

$$\Delta\sigma(\omega) = \frac{\varepsilon_0 c\alpha(n_0^2 - n_1^2)}{2}\left(1 - \mathrm{i}\frac{2\omega n_0}{\alpha c}\right)\left(\frac{\Delta R}{R}\right), \tag{6}$$

where α is the absorption coefficient of $MAPbI_3$ at 400 nm and n_0 is the refractive index of $MAPbI_3$ at THz frequencies and n_1 is the refractive index of surrounding medium (sapphire for low temperature measurements). Detailed derivation of equation (6) is given in the supplemental material. $\Delta R = R_{\mathrm{on}} - R_{\mathrm{off}}$ is the difference in reflected THz electric field with and without photoexcitation. In contrast to equation (4), this expression is less straightforward to apply owing to the complexity arising from the potential phase change of the THz pulse upon reflection at the sapphire–perovskite interface. According to the thin-film approximation which is also valid for $MAPbI_3$ single crystal since $2\omega n_0/\alpha c \ll 1$, the photoconductivity of $MAPbI_3$ single crystal is linearly proportional to $\Delta R/R$ and therefore in figures 3(c) and (d), $\Delta R/R$ was plotted as a simplified representation of the photoconductivity.

Since the photoconductivity arises from the generation of free charge carriers in the semiconductor material via the absorption of incident photons, it reveals the fundamental structural and optoelectronic properties of the material under investigation. Here, we utilized the time-resolved OPTPS technique to measure the photoconductivity spectra of $MAPbI_3$ (figure 3) on a picosecond timescale (5 ps after photoexcitation), which were found to contain the signature of ultrafast photo-induced phonon hardening. As will be discussed later, based on our first-principles calculations, this phenomenon is attributed to an electronic process, in contrast to the previously reported lattice structural change [49, 50] which happens on a much slower timescale.

Considering the photoconductivity of single-crystal $MAPbI_3$ at room temperature, which is displayed in figure 3(c), there is a feature that appears to be the derivative of the dark conductivity spectrum (figure 1(b)) superimposed on a flat free charge carrier (Drude) response. The derivative-like feature arises for a blue-shifting of the phonon frequency as a result of illumination, that is

$$\begin{aligned}\Delta\sigma(\omega) &= \sigma_{\mathrm{photoexcitation}}(\omega) - \sigma_{\mathrm{dark}}(\omega)\\ &= [\sigma_{\mathrm{dark}}(\omega + \Delta\omega) + \sigma_{\mathrm{Drude}}] - \sigma_{\mathrm{dark}}(\omega)\\ &\approx \sigma_{\mathrm{Drude}} + \frac{\mathrm{d}\sigma_{\mathrm{dark}}}{\mathrm{d}\omega}\Delta\omega\end{aligned} \tag{7}$$

where the dark conductivity σ_{dark} (figure 1) characterizes the phonon modes and the frequency-shift term ($\frac{\mathrm{d}\sigma_{\mathrm{dark}}}{\mathrm{d}\omega}\Delta\omega$) resembles the shape of the real part of photoconductivity shown in figure 3(b). The grey dashed vertical line in figure 3(c) indicates the frequency of the Pb–I stretch TO phonon mode as determined from the dark conductivity spectrum (figure 1(b)) and clearly illustrates the photo-induced blueshifting of the mode according to equation (7). A similar blueshift can be seen for each phonon mode in the mode-rich low-temperature photocondutivity spectra of both thin-film and single-crystal $MAPbI_3$ as shown in figures 3(b) and (d) respectively.

Phonon blueshifting effects have also been observed in formamidinium perovskite thin films [51] and $MAPbI_3$ nanocrystals [52], where a combined model of Drude-Smith and peak-shift contributions was applied [51], and the photoconductivity spectrum was found to be sensitive to both the phonon oscillator strength and resonant frequency. Based on ultrafast electron diffraction measurement of $MAPbI_3$ thin films [49] and the anharmonic electron–phonon coupling predicted by DFPT [53] a change of phonon profile was claimed to come from the ionic displacement under photoexcitation. The blueshift of phonon frequency in $MAPbI_3$ has been investigated by various studies, according to which the common conclusion is that blueshift in phonon modes arises from a lattice structural change [50]. However, since our THz spectroscopy measurement is performed on an ultrafast timescale (on the order of a few picoseconds), such a phonon hardening effect is unlikely to originate from a lattice structural change but more likely from an electronic process [49].

To gain deeper insight into the origin of this observed phonon hardening we performed density-functional theory (DFT) calculations using pseudopotentials and plane waves to calculate phonons with considerations of spin–orbit coupling. The MA^+ cation was replaced with Cs^+ cation to reduce the computational cost and preserve isotropic average. Since the main phonon mode probed in the THz spectroscopy measurements is the Pb–I stretching mode, the librations of the MA^+ cation is not

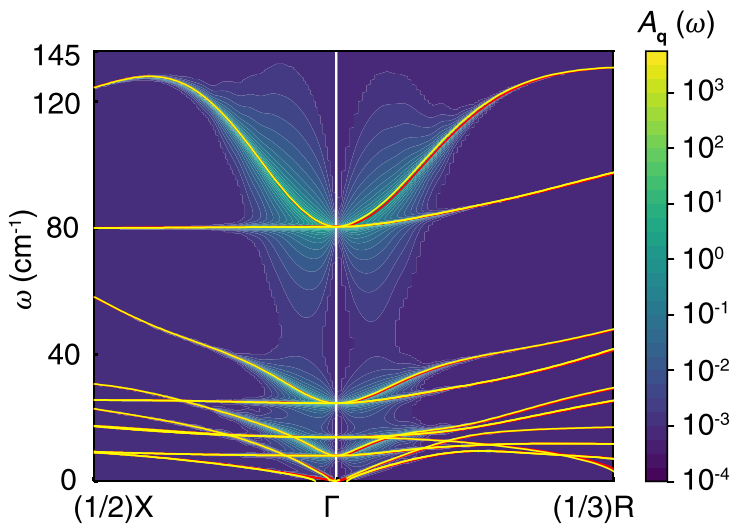

Figure 4. Calculated phonon dispersion for $CsPbI_3$ with 10^{17} cm^{-3} electron doping using a lattice parameter of $a = 6.276$ Å. The phonon spectral function $A_{\mathbf{q}}(\omega)$ is non-adiabatic and computed at 300 K with the renormalized phonon frequencies $\Omega_{\mathbf{q},\nu}$, defined in equation (S19) of the supplemental material, indicated by yellow lines. The red lines are the DFPT adiabatic phonon frequencies $\omega_{\mathbf{q},\nu}$.

involved [18] and hence less relevant. On top of that, Cs^+ is also the largest elemental cation in the periodic table, which is the closest approximation to the MA^+ cation in terms of steric size. Therefore, it is reasonable to use the phonon dispersion relations and vibrational eigenmodes of $CsPbI_3$ as an approximation for $MAPbI_3$. The computed many-body electronic band structure of $CsPbI_3$ is shown in supplementary figure 7 with a bandgap of 0.86 eV. A rigid band approximation was used to simulate photo-injected electron–hole pair density (i.e. optical 'doping' density) induced via photoexcitation in the OPTPS measurement, including the effect of temperature through the non-adiabatic phonon self-energy and spectral function [54], which is exemplified in figure 4 with electron density of $10^{17}cm^{-3}$ (spectral functions calculated at other doping densities are given in the supplemental material).

Table 2 lists a few representative phonon modes obtained from the DFT calculations under conditions of undoped, hole doping density $10^{17}cm^{-3}$ and electron doping density $10^{17}cm^{-3}$ respectively. A more complete table with different doping density values (e.g. 10^{18} and $10^{19}cm^{-3}$) is provided in the supplemental material. In the DFT calculations for $CsPbI_3$, the highest TO mode with $\omega_{TO} = 81$ cm^{-1} corresponds to the Pb–I stretching mode, which exhibits a phonon hardening effect at electron/hole doping density of $10^{17}cm^{-3}$.

In order to capture the extent to which photoexcitation leads to a hardening of phonon modes, we simulated the photoexcitation condition for $CsPbI_3$ at different electron doping densities. The highest TO mode, which is regarded as the representative mode for the Pb–I stretching phonon mode in $MAPbI_3$, shows a phonon hardening of 0.31, 0.56 and 0.64 cm^{-1} at electron doping densities of 10^{17}, 10^{18} and $10^{19}cm^{-3}$ respectively. This suggests that the phonon hardening effect is stronger at larger electron density due to the Pauli blocking effect where a change in the occupation numbers of the electrons upon photoexcitation makes certain virtual processes in equation (S17) allowed/forbidden (as compared to the system without photoexcitation). The modeling also showed that photoexcitation leads to a light induced contraction of the lattice, that is 'photostriction'. For steady-state photo-doping of 10^{19} cm^{-3}, the lattice parameter was calculated to contract from 6.381 to 6.363 Å and further harden the TO mode by $\sim$3 cm^{-1}. However in the experiments phonon modes were recorded just 5 ps after photoexcitation, so such global lattice contraction is not expected to be observed as it would occur on much longer timescales.

To correlate the theoretical results with our experimental results, we compare the phonon hardening values measured to those calculated at similar electron densities. In the experiment on single-crystal $MAPbI_3$, a phonon hardening of $\sim$0.33 cm^{-1} was observed at photoexcitation fluence 48 μJ cm^{-2} which corresponds to an electron density around 7.5×10^{18} cm^{-3} based on the absorption coefficient of $MAPbI_3$ at 400 nm [55]. The calculated phonon hardening of a doping density of 10^{18} cm^{-3} (i.e. 0.56 cm^{-1} shown in table 3) is consistent with the experimental result, given the spectral resolution of the experiment.

Another interesting point noticed in the theoretical calculation is that although the Pb–I–Pb bending mode ($\omega_{TO} = 27.5cm^{-1}$) of $CsPbI_3$ shows a phonon-softening effect (redshift of phonon frequency), the magnitude of such phonon softening decreases with increasing electron doping density. This indicates that higher electron doping density, which is equivalent to the enhancement of phonon-hardening effect at higher

Table 2. Renormalized frequencies of the highest TO mode, mid TO modes 10–11 and mid TO modes 7–8 calculated at the zone center for $CsPbI_3$ at temperature 300 K (unit:cm^{-1}).

	Highest TO Pb–I stretching	Mid-TO (modes 10–11) Pb–I–Pb bending	Mid-TO (modes 7–8) A-site displacement
Undoped	81.0186	27.4562	13.4219
h^+ doping (10^{17} cm^{-3})	81.1353	24.8777	14.0419
e^- doping (10^{17} cm^{-3})	81.2164	23.8275	13.4742

Table 3. Theoretically calculated values of phonon hardening (positive number) or phonon softening (negative number) in cm^{-1} as a function of doping for three TO modes associated with Pb–I stretching, Pb–I–Pb bending and A-site displacement in $CsPbI_3$. The effect includes adiabatic and non-adiabatic effects (at 300 K).

	Highest TO Pb–I stretching	Mid-TO (modes 10–11) Pb–I–Pb bending	Mid-TO (modes 7–8) A-site displacement
Undoped	81.0186	27.4562	13.4219
Doping 10^{17} cm^{-3}	+0.3145	−6.2072	+0.6723
Doping 10^{18} cm^{-3}	+0.5647	−6.0362	+0.8177
Doping 10^{19} cm^{-3}	+0.6446	−5.8746	+1.1404

electron density. Overall, both the experimental and theoretical results show a phonon hardening effect in the presence of photo-induced electrons. According to our calculations, this phonon hardening phenomenon arises from the Pauli blocking effect resulting from the electron doping, which is achieved by photoexcitation in experiment. This phonon-hardening effect is an electronic process which happens on an ultrafast (sub-picosecond) timescale. The possibility of it originating from a light-induced lattice structural change is low, since such process tends to happen on a much longer timescale [23, 24].

3. Conclusion

In conclusion using a combination of experiment and theory we have performed a direct comparison of Pb–I stretching phonon modes between single-crystal and thin-film polycrystalline $MAPbI_3$ as a function of both temperature and illumination level. Phonon modes observed in $MAPbI_3$ thin film showed a blue-shift trend with increasing temperature, while in contrast, the phonon frequency remained constant in single crystal. At higher temperatures, both single crystal and thin film exhibited broadened phonon linewidths, which was attributed to the structural disorder. Single crystal was found to have a much lower phonon scattering rate and longer phonon lifetime than polycrystalline $MAPbI_3$. Phonon scattering in $MAPbI_3$ single crystals was attributed to anharmonicity and optical phonon–electron (Fröhlich) interactions, which places the primary limit to the charge-carrier mobility in single crystals. $MAPbI_3$ polycrystalline thin films exhibited additional phonon scattering associated with increased crystalline disorder as a result of grain boundaries, strain and impurities, which is the reason why polycrystalline $MAPbI_3$ tends to have a significantly lower charge-carrier mobility than single crystals.

Moreover, anomalous hardening of TO phonon modes in $MAPbI_3$ was observed following above-bandgap photoexcitation, which contrasts to the mode softening expected for most semiconductors when photoexcited. Our non-adiabatic DFT calculations predicted a similar degree of mode hardening and allowed us to assign the hardening mechanism to Pauli blocking following the photo-injection of charge carriers. The mode hardening in $MAPbI_3$ occurred on an ultrafast (picosecond) timescale and was found to be distinct from global lattice contraction (photostriction) which occurs over a longer timescale. This work highlights the importance of electron–phonon coupling in $MAPbI_3$ and the strong connection between vibrational modes and the electronic and optical properties of this remarkable semiconductor.

4. Methods

4.1. Sample fabrications

$MAPbI_3$ single crystal: The $MAPbI_3$ perovskite single crystals were prepared by inverse temperature crystallization [25, 26]. Typically, 1.25 M $MAPbI_3$ precursor was prepared by adding 461 mg PbI_2 and 159 mg methylammonium iodide (MAI) into 0.8 ml γ-butyrolactone, heated at 60 °C for 2 hours with stirring. The precursors were filtered with syringe filters (0.22 μm pore size). The obtained solution was transferred to clean containers, which were kept on a stable hot-plate and gradually heated to 120 °C and

kept for another 6 hours. Crystals were formed in the bottom of the containers. Finally, the crystals were collected and dried at 60 °C in a vacuum oven for 12 hours.

$MAPbI_3$ thin film: Polycrystalline $MAPbI_3$ thin films of 600 nm thickness were grown on 13 mm diameter, 2 mm thick z-cut quartz disc [34]. (1) Cleaning of substrate: z-cut quartz substrates were cleaned with hellmanex solution, followed by a thorough rinse with deionized water. The substrate was then washed with acetone, isopropanol, and ethanol. Thereafter the substrates were plasma etched in O_2 for 10 min. (2) Thermal co-evaporation of $MAPbI_3$: the $MAPbI_3$ was fabricated using thermal evaporation as reported previously [28, 29]. In brief, MAI and PbI_2 were placed in separate crucibles, and the substrates were mounted on a rotating substrate holder to ensure that a uniform film was deposited. The temperature of the substrates was kept at 21 °C throughout the deposition. The chamber was evacuated to reach a high vacuum ($\approx 10^{-6}$ mbar), before heating the PbI_2 and the MAI. The substrates were then exposed to the vapor. The rates of both the MAI and PbI_2 were monitored using a quartz-crystal microbalance. The thickness of the perovskite thin film was set by controlling the exposure time of the substrates to the vapor.

4.2. Experimental methods

THz-TDS: THz time-domain spectroscopy was utilized to measure the phonon modes of $MAPbI_3$ thin films and single crystals. The THz pulse was generated by a THz spintronic emitter via the inverse spin Hall effect [56]. An amplified ultrafast (35 fs) laser beam with an average power of 4 W, repetition rate of 5 kHz and central wavelength of 800 nm was split into two arms: a probe (THz) beam and a gate beam to detect the THz signal using electro-optic sampling. A 1 mm-thick (110) ZnTe crystal was used as the THz detector together with a Wollaston prism and a pair of balanced photodiodes. The reflection of THz pulse was redirected by a Si beam splitter and detected by another set of a Wollaston prism, a 1 mm-thick (110) ZnTe crystal and a pair of photodiodes. The temperature-dependent conductivity measurement was performed by mounting the thin film and single crystal on a cold-finger cryostat (Oxford Instruments, MicrostatHe), which was able to cool down to 5 K. A schematic diagram of the THz spectroscopy setup is provided in the supplemental material.

OPTPS: Optical-pump-terahertz-probe spectroscopy is an extension of the THz-TDS with the introduction of an extra pump beam. The pump beam is a third beam path that splits off the amplified laser, which is then frequency-doubled to 400 nm by a β-barium-borate (BBO) crystal. A detailed schematic diagram of the THz-TDS and OPTPS setups is given in the supplemental material. Under photoexcitation with the pump beam, free charge carriers are generated in the $MAPbI_3$ perovskite, which reduces the transmission (or increases the reflectivity) of the THz signal. The change of THz intensity is related to the photoconductivity as indicted by equations (4) and (6). In our experiment, the time delay between the peaks of the pump beam and the THz beam was fixed, and the photoconductivity spectra were measured at 5 ps after photoexcitation.

Temperature-dependent PL spectroscopy: We performed temperature-dependent PL measurements on the $MAPbI_3$ single crystal to determine its true temperature based on the evolution of PL spectra over a temperature range of 5–300 K. The PL spectra were generated by the pump beam at 400 nm and single crystal's temperature was controlled by a cold-finger cryostat. The emitted PL spectrum was collected by a fibre-coupled spectrometer (Horiba Scientific, iHR320) and detected by a CCD (Horiba Scientific, Si Symphony II). To improve the thermal conductivity between the $MAPbI_3$ single crystal and the cold-finger cryostat, a sapphire substrate was inserted at the front of the single crystal to dissipate the excess heat generated by the pump beam. To measure the single crystal's temperature accurately, a PL-facilitated temperature correction technique [7] was developed where by the temperature-dependent PL spectra were measured again using a gas-exchange cryostat (Oxford Instruments, OptistatCF2). Since in this setup the single crystal was immersed in helium gas, there was no thermal contact issue and the temperature detected by the gas-exchange cryostat was assumed to be the true temperature of the single crystal. The PL spectra measured by the gas-exchange cryostat were therefore used as a reference to correct the temperature of single crystal via the comparison with the PL spectra measured by the cold-finger cryostat. As a result, the single crystal was found to reach a minimum temperature of 75 K. The PL spectra measured in the gas-exchange cryostat setup were generated by a picosecond pulsed diode laser (PicoHarp, LDH-D-C-405M) at central wavelength of 398 nm and fluence 210 nJ cm^{-2}. The signal was collected and coupled into a different spectrometer (Princeton Instruments, SP-2558), and detected by an iCCD (Princeton Instruments, PI-MAX4).

4.3. Computational methods

We approximated cubic $MAPbI_3$ by $CsPbI_3$ using the cubic $MAPbI_3$ lattice parameters of $a = 6.276$ Å [37]. We performed DFT calculations using pseudopotentials and planewaves, as implemented in the Quantum ESPRESSO package [57]. We used the PBE generalized gradient approximation with norm-conserving

pseudopotentials from the PseudoDojo repository [58]. We used fully relativistic pseudopotentials which include the effect of spin–orbit coupling as well as including semicore 5s, 5p, and 5d electrons in the case of Pb. We used a planewaves kinetic energy cutoffs of 100 Ry. We calculated the phonons using density-functional perturbation theory [59] with dense $16 \times 16 \times 16$ k-points and $8 \times 8 \times 8$ q-points grid. We corrected DFT band structures via the quasiparticle GW method, using the Yambo code [60]. We employed a higher planewaves kinetic energy cutoff of 150 Ry, we evaluated the exchange self-energy and the polarisability using cutoffs of 60 and 15 Ry, respectively, and performed the summations over empty states using 500 bands for the calculation of the polarization, and 600 bands for the Green's function. The frequency-dependence of the screened Coulomb interaction was described via the Godby–Needs plasmon-pole model [61], using a plasmon-pole energy of 18.8 eV. Since the DFT gap of perovskites is small due to spin–orbit coupling [62], we went beyond the G_0W_0 approximation by including self-consistency on the eigenvalues. We apply self-consistency by using a strategy similar to [62], but with a wavevector-dependent scissor so as to obtain accurate effective masses. The Brillouin zone was sampled via a $8 \times 8 \times 8$ unshifted grid, and the termination scheme of [63] was employed to accelerate the convergence with respect to the number of empty states. We interpolated the electron-phonon matrix elements from coarse $8 \times 8 \times 8$ k/q grids to a dense R-centered Cauchy grids for phonons with 105 000 points using the EPW code [64, 65] of the Quantum ESPRESSO distribution, in conjunction with the wannier90 library [66]. We included spin–orbit coupling in all calculations.

Data availability statement

The data that support the findings of this study are available upon reasonable request from the authors.

Acknowledgments

This work was funded by the Engineering and Physical Sciences Research Council (EPSRC). M B J thanks the Alexander von Humboldt Foundation for support. S P acknowledges the support from the European Union's Horizon 2020 Research and Innovation Programme, under the Marie Skłodowska-Curie Grant Agreement SELPH2D No. 839217. F G 's contribution was supported as part of the Computational Materials Sciences Program funded by the U.S. Department of Energy, Office of Science, Basic Energy Sciences, under Award DE-SC0020129. L M H thanks the Institute for Advanced Study at the Technical University of Munich for support through a Hans Fischer Senior Fellowship. CQX performed the THz measurements, temperature-dependent PL measurements, undertook the data analysis and participated in the experimental planning. J P prepared the single-crystal samples. S P carried out the first-principles calculations. J B P prepared the thin-film samples. A M U provided support with the THz spectrum analysis. A D W provided support with the temperature-dependent PL measurements. R L M provided support with the THz experimental setup. H K developed the electronics and firmware for THz data acquisition. This project was conceived, planned and supervised by Q L, F G, L M H and M B J. C Q X and M B J prepared the manuscript while all authors discussed and commented on it.

Conflict of interest

The authors declare no financial conflicts of interest.

ORCID iDs

Chelsea Q Xia https://orcid.org/0000-0001-7920-6973
Samuel Poncé https://orcid.org/0000-0003-1159-8389
Adam D Wright https://orcid.org/0000-0003-0721-7854
Qianqian Lin https://orcid.org/0000-0002-6144-1761
Laura M Herz https://orcid.org/ 0000-0001-9621-334X
Michael B Johnston https://orcid.org/0000-0002-0301-8033

References

[1] NREL best research-cell efficiencies (available at: www.nrel.gov/pv/cell-efficiency.html/) (Accessed 11 February 2021)
[2] Kojima A, Teshima K, Shirai Y and Miyasaka T 2009 *J. Am. Chem. Soc.* **131** 6050–1
[3] Wehrenfennig C, Eperon G E, Johnston M B, Snaith H J and Herz L M 2014 *Adv. Mater.* **26** 1584–9
[4] Wehrenfennig C, Liu M, Snaith H J, Johnston M B and Herz L M 2014 *Energy Environ. Sci.* **7** 2269–75

[5] Milot R L, Eperon G E, Snaith H J, Johnston M B and Herz L M 2015 *Adv. Funct. Mater.* **25** 6218–27
[6] Herz L M 2017 *ACS Energy Lett.* **2** 1539–48
[7] Xia C Q *et al* 2021 *J. Phys. Chem. Lett.* **12** 3607–17
[8] Egger D A *et al* 2018 *Adv. Mater.* **30** 1800691
[9] Yaffe O *et al* 2017 *Phys. Rev. Lett.* **118** 136001
[10] Jacobsson T J, Schwan L J, Ottosson M, Hagfeldt A and Edvinsson T 2015 *Inorg. Chem.* **54** 10678–85
[11] Wright A D, Verdi C, Milot R L, Eperon G E, Pérez-Osorio M A, Snaith H J, Giustino F, Johnston M B and Herz L M 2016 *Nat. Commun.* **7** 11755
[12] Poncé S, Li W, Reichardt S and Giustino F 2020 *Rep. Prog. Phys.* **83** 036501
[13] Quarti C, Grancini G, Mosconi E, Bruno P, Ball J M, Lee M M, Snaith H J, Petrozza A and De Angelis F 2013 *J. Phys. Chem. Lett.* **5** 279–84
[14] Ledinský M, Löper P, Niesen B, Holovský J, Moon S J, Yum J H, De Wolf S, Fejfar A and Ballif C 2015 *J. Phys. Chem. Lett.* **6** 401–6
[15] Onoda-Yamamuro N, Matsuo T and Suga H 1990 *J. Phys. Chem. Solids* **51** 1383–95
[16] Mosconi E, Quarti C, Ivanovska T, Ruani G and De Angelis F 2014 *Phys. Chem. Chem. Phys.* **16** 16137–44
[17] Glaser T *et al* 2015 *J. Phys. Chem. Lett.* **6** 2913–18
[18] Pérez-Osorio M A, Milot R L, Filip M R, Patel J B, Herz L M, Johnston M B and Giustino F 2015 *J. Phys. Chem.* C **119** 25703–18
[19] Pérez-Osorio M A, Lin Q, Phillips R T, Milot R L, Herz L M, Johnston M B and Giustino F 2018 *J. Phys. Chem.* C **122** 21703–17
[20] Zijlstra E S, Tatarinova L L and Garcia M E 2006 *Phys. Rev.* B **74** 220301
[21] Stampfli P and Bennemann K H 1990 *Phys. Rev.* B **42** 7163–73
[22] Recoules V, Clérouin J, Zérah G, Anglade P M and Mazevet S 2006 *Phys. Rev. Lett.* **96** 055503
[23] Zhou Y, You L and Wang S *et al* 2016 *Nat. Commun.* **7** 11193
[24] Wei T C, Wang H P, Li T Y, Lin C H, Hsieh Y H, Chu Y H and He J H 2017 *Adv. Mater.* **29** 1701789
[25] Saidaminov M I *et al* 2015 *Nat. Commun.* **6** 7586
[26] Peng J, Cui L, Li R, Xu Y, Jiang L, Li Y, Li W, Tian X and Lin Q 2019 *J. Mater. Chem.* C **7** 1859–63
[27] Liu M, Johnston M B and Snaith H J 2013 *Nature* **501** 395–8
[28] Lohmann K B, Patel J B, Rothmann M U, Xia C Q, Oliver R D J, Herz L M, Snaith H J and Johnston M B 2020 *ACS Energy Lett.* **5** 710–17
[29] Patel J B *et al* 2020 *Adv. Energy Mater.* **10** 1903653
[30] Wang M and Lin S 2016 *Adv. Funct. Mater.* **26** 5297–306
[31] Pisoni A, Jacimovic J, Barisic O S, Spina M, Gaál R, Forró L and Horváth E 2014 *J. Phys. Chem. Lett.* **5** 2488–92
[32] Nienhuys H K and Sundström V 2005 *Phys. Rev.* B **71** 235110
[33] Lloyd-Hughes J and Jeon T I 2012 *J. Infrared Millim. Terahertz Waves* **33** 871–925
[34] Davies C L, Patel J B, Xia C Q, Herz L M and Johnston M B 2018 *J. Infrared Millim. Terahertz Waves* **39** 1236–48
[35] Naftaly M and Dudley R 2011 *Appl. Opt.* **50** 3201–4
[36] Weller M T, Weber O J, Henry P F, Di Pumpo A M and Hansen T C 2015 *Chem. Commun.* **51** 4180–3
[37] Baikie T, Fang Y, Kadro J M, Schreyer M, Wei F, Mhaisalkar S G, Graetzel M and White T J 2013 *J. Mater. Chem.* A **1** 5628–41
[38] La-o vorakiat C *et al* 2016 *J. Phys. Chem. Lett.* **7** 1–6
[39] Zhao D *et al* 2017 *Appl. Phys. Lett.* **111** 201903
[40] Zhu C *et al* 2019 *Nat. Commun.* **10** 815
[41] Korlacki R, Stokey M, Mock A, Knight S, Papamichail A, Darakchieva V and Schubert M 2020 *Phys. Rev.* B **102** 180101
[42] Whalley L D, Skelton J M, Frost J M and Walsh A 2016 *Phys. Rev.* B **94** 220301
[43] Perez-Osorio M A, Champagne A, Zacharias M, Rignanese G M and Giustino F 2017 *J. Phys. Chem.* C **121** 18459–71
[44] Rothmann M U *et al* 2020 *Science* **370** eabb5940
[45] La-o Vorakiat C, Cheng L, Salim T, Marcus R A, Michel-Beyerle M E, Lam Y M and Chia E E 2017 *Appl. Phys. Lett.* **110** 123901
[46] Ulatowski A M, Herz L M and Johnston M B 2020 *J. Infrared Millim. Terahertz Waves* **41** 1431–49
[47] D'Angelo F, Němec H, Parekh S H, Kužel P, Bonn M and Turchinovich D 2016 *Opt. Express* **24** 10157–71
[48] Hempel H, Unold T and Eichberger R 2017 *Opt. Express* **25** 17227–36
[49] Wu X *et al* 2017 *Sci. Adv.* **3** e1602388
[50] Huang W *et al* 2018 *ACS Photonics* **5** 1583–90
[51] Zhao D *et al* 2019 *ACS Nano* **13** 8826–35
[52] La-o-vorakiat C, Salim T and Kadro J *et al* 2015 *Nat. Commun.* **6** 7903
[53] Whalley L D, Skelton J M, Frost J M and Walsh A 2016 *Phys. Rev.* B **94** 220301
[54] Giustino F 2017 *Rev. Mod. Phys.* **89** 015003
[55] De Wolf S, Holovsky J, Moon S J, Löper P, Niesen B, Ledinsky M, Haug F J, Yum J H and Ballif C 2014 *J. Phys. Chem. Lett.* **5** 1035–9
[56] Seifert T, Jaiswal S, Sajadi M, Jakob G, Winnerl S, Wolf M, Kläui M and Kampfrath T 2017 *Appl. Phys. Lett.* **110** 252402
[57] Giannozzi P *et al* 2017 *J. Phys. Condens. Matter* **29** 465901
[58] van Setten M J, Giantomassi M, Bousquet E, Verstraete M, Hamann D, Gonze X and Rignanese G M 2018 *Comp. Phys. Comm.* **226** 39–54
[59] Gonze X and Lee C 1997 *Phys. Rev.* B **55** 10355–68
[60] Marini A, Hogan C, Grüning M and Varsano D 2009 *Comp. Phys. Commun.* **180** 1392–403
[61] Godby R W and Needs R J 1989 *Phys. Rev. Lett.* **62** 1169–72
[62] Davies C L *et al* 2018 *Nat. Commun.* **9** 293
[63] Bruneval F and Gonze X 2008 *Phys. Rev.* B **78** 085125
[64] Poncé S, Margine E R, Verdi C and Giustino F 2016 *Comp. Phys. Commun.* **209** 116–33
[65] Giustino F, Cohen M L and Louie S G 2007 *Phys. Rev.* B **76** 165108
[66] Pizzi G *et al* 2020 *J. Phys. Condens. Matter* **32** 165902